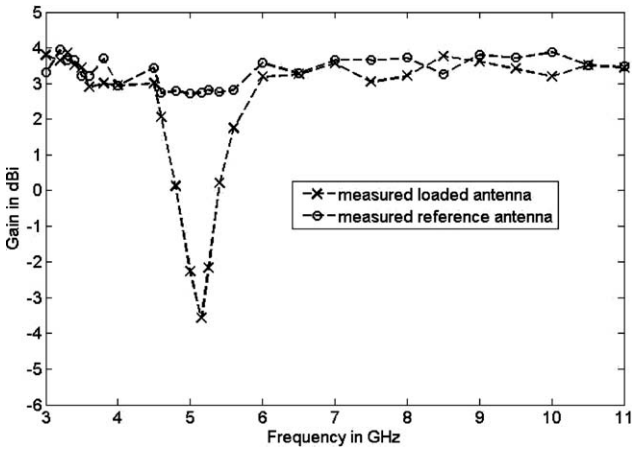


**Figure 6** Measured peak gain for slotted antenna with 0.75 pF loading capacitor and reference antenna

The simulated patterns were generated using CST software packages, while the measurement were taken in an anechoic chamber using a calibrated EMCO type 3115 broadband horn as a reference antenna. As can be seen, the antenna gives a nearly omnidirectional and consistent radiation pattern across the operating frequency band.

The measured peak gains for the band-rejected (with capacitor of 0.75 pF) and standard UWB (without capacitor) antennas are plotted in Figure 6. The standard UWB antenna has an average peak gain of 3 dBi across the band. As for the band-rejected antenna, the fluctuation of the average peak gain is similar to the standard UWB antenna except the at the band-notched frequency band (5.15–5.75 GHz), where a gain suppression of ~6.3 dB can be seen.

## 4. CONCLUSIONS

An UWB antenna with band-notched behavior has been implemented by loading the PIFLA antenna with different capacitance values. In practice, a varactor diode would be used to enable electronic tuning. By means of a control signal, the notch band center frequency could then easily be tuned from 3.2 to 6 GHz, while experimental results show the fabricated antenna has a nearly omnidirectional radiation pattern with good gain suppression. By balancing the size and bandwidth constraints, the proposed antenna occupies a compact envelope dimension of 30 × 15 × 5 mm$^3$, while covering the required UWB operating frequency bands with a targeted rejection band.

## REFERENCES


1. D. Geer, UWB Standardization effort ends in controversy, Computer 39 (2006), 13–16.
2. M. Hamalainen, A. Taparugssanagorn, R. Tesi, and J. Iinatti, Wireless medical communications using UWB, In the Proceeding of IEEE International Conference on Ultra-Wideband ICUWB 2009, September 2009, pp.485–489.
3. Revision of Part 15 of the Communication's Rules Regarding Ultra-Wideband Transmission Systems, Federal Communications Commission, Washington, DC, ET-Docket 98-153, FCC 02-48, 2002.
4. N.D. Trang, D.H. Lee, and H.C. Park, Compact printed CPW-fed monopole ultra-wideband antenna with triple sub-band notched characteristics, Electron Lett 46 (2010), 1177–1179.
5. A.J. Kerkhoff and H. Ling, Design of a band-notched planar monopole antenna using genetic algorithm optimisation, IEEE Trans Antennas Propag AP-55 (2007), 604–610.
6. K.H. Kim, Y.J. Cho, S.H. Hwang, and S.O. Park, Band-notched UWB planar monopole antenna with two parasitic patches, Electron Lett 41 (2005), 783–785.
7. V.A. Shameena, M.N. Suma, K. Raj Rohith, P.C. Bybi, and P. Mohanan, Compact ultra-wideband serrated antenna with notch band ON/OFF control, Electron Lett 42 (2006).
8. B. Rahmati and H.R. Hassani, Wideband planar plate monopole antenna with dual tunable notch, Electron Lett 46 (2010), 480–481.
9. Z.H. Hu, P.S. Hall, J.R. Kelly, and P. Gardner, UWB pyramidal monopole antenna with wide tunable band-notched behaviour, Electron Lett 46 (2011), 1588–1590.
10. C.H. See, R.A. Abd-Alhameed, D. Zhou, H.I. Hraga, P.S. Excell, and M.B. Child, An ultra-wideband planar inverted FF antenna, Electron Lett 46 (2010), 549–550.
11. C.H. See, R.A. Abd-Alhameed, H.I. Hraga, I.T. E. Elfergani, M.M. Abusitta, and S. Adnan, Design of a PIFA with parasitic F-element miniaturised antenna assembly for lower band ultra-wideband and IEEE 802.11a applications, Microwave Opt Technol Lett 53 (2011), 1970–1974.
12. CST v.5.0, Microwave Studio, Wellesley Hills, MA, http://www.cst.com/.


© 2012 Wiley Periodicals, Inc.

# LARGE ANISOTROPIC INHOMOGENEOUS HIGHER ORDER HIERARCHICAL GENERALIZED HEXAHEDRAL FINITE ELEMENTS FOR 3-D ELECTROMAGNETIC MODELING OF SCATTERING AND WAVEGUIDE STRUCTURES

**Ana B. Manić,[1] Sanja B. Manić,[1] Milan M. Ilić,[1,2] and Branislav M. Notaroš[1]**
[1] Department of Electrical and Computer Engineering, Colorado State University, Fort Collins, CO 80523-1373; Corresponding author: notaros@colostate.edu
[2] University of Belgrade, School of Electrical Engineering, 11120 Belgrade, Serbia

*Received 10 September 2011*

**ABSTRACT:** *A higher order large-domain finite element technique for three-dimensional modeling of electromagnetic structures involving general anisotropic inhomogeneous materials is presented. The examples demonstrate efficient and accurate simulations of scattering and waveguide structures using large (a couple of wavelengths across) anisotropic continuously inhomogeneous curved finite elements with* p-*refined (high-order) field distributions.* © 2012 Wiley Periodicals, Inc. Microwave Opt Technol Lett 54:1644–1649, 2012; View this article online at wileyonlinelibrary.com. DOI 10.1002/mop.26892

**Key words:** *finite element method; anisotropic inhomogeneous materials; higher order modeling; scattering; waveguide discontinuities*

## 1. INTRODUCTION

The finite element method (FEM) is one of the most powerful and versatile general numerical tools for solving both open-region (e.g., antenna/scattering) and closed-region (e.g., waveguide/cavity) problems in electromagnetics [1–4]. It has been especially effectively used in three-dimensional (3D) frequency-domain modeling and analysis of electromagnetic structures that contain geometrical and material complexities. In terms of the particulars of the numerical discretization, conversely, traditional FEM tools are low-order (also referred to as small-domain or subdomain) techniques – the electromagnetic structure is modeled by volume geometrical elements that are electrically very small and with planar sides, and the fields within the elements

are approximated by low-order basis functions, which results in very large requirements in computational resources. An alternative which can greatly reduce the number of unknowns for a given problem and enhance the accuracy and efficiency of the FEM analysis is the higher order (also known as the large-domain or entire-domain) computational approach, which uses higher order basis functions defined in large-curved geometrical elements [5]. However, although higher order FEM modeling has, since relatively recently, been constantly gaining popularity among FEM developers and practitioners and is definitely becoming a mainstream activity in FEM research and practice, there seems to be a lack of investigations and reported results on the actual higher order and large-domain modeling of material complexities and a full exploitation of modeling flexibility and efficiency of large curved finite elements with $p$-refined high-order field approximations when applied in the presence of arbitrary material anisotropy and inhomogeneity.

This article presents a novel higher order large-domain FEM technique for efficient and accurate 3D analysis in the frequency domain of open- and closed-region electromagnetic structures involving general anisotropic inhomogeneous materials, as an extension and generalization of works in [6–9]. The technique implements Lagrange-type generalized curved parametric hexahedral finite elements of arbitrary geometrical-mapping orders, filled with anisotropic inhomogeneous materials with continuous spatial variations of complex relative permittivity and permeability tensors described by Lagrange interpolation polynomials of arbitrary material-representation orders, and curl-conforming hierarchical polynomial vector basis functions of arbitrary field-expansion orders for the approximation of the electric field vector within the elements. The technique is applied to the analysis of open-region scattering structures, with a truncation of the FEM domain by a hybridization with a higher order method of moments (MoM) within the surface integral equation (SIE) approach [10, 8], and to the analysis of closed-region microwave waveguide structures, with a simple single-mode boundary condition introduced across the waveguide ports and a large buffer finite element at each port to ensure relaxation of higher modes [7]. To the best of our knowledge, this is the first demonstration of large (extending a couple of wavelengths in each dimension) anisotropic inhomogeneous curved finite elements with $p$-refined field distributions of high (e.g., seventh) approximation orders in high-frequency electromagnetics. Our current and future related work includes applications of these new elements in analysis and design of anisotropic inhomogeneous dielectric and magnetic material structures aimed for (i) electromagnetic cloaking [13], (ii) perfectly matched layers (PMLs) [2], and (iii) waveguide components.

## 2. THEORY AND IMPLEMENTATION

Consider an electromagnetic structure that contains some anisotropic continuously inhomogeneous material regions. In our analysis method, the computational domain is first tessellated using higher order geometrical elements, and the electric field intensity vector within the $e$th element is approximated by the following sum:

$$\mathbf{E}^e = \sum_{l=1}^{N^e} \gamma_l^e \, \mathbf{f}_l^e, \tag{1}$$

where $\mathbf{f}_l$ are higher order vector basis functions with a total of $N^e$ unknown field-distribution coefficients $\gamma_l$ in the element. Elements are adopted in the form of Lagrange-type generalized curved parametric hexahedra of arbitrary geometrical orders $K_u^e$, $K_v^e$, and $K_w^e$ ($K_u^e$, $K_v^e$, $K_w^e \geq 1$), shown in Figure 1 and analytically described as [6]

$$\mathbf{r}^e(u,v,w) = \sum_{i=0}^{K_u^e} \sum_{j=0}^{K_v^e} \sum_{k=0}^{K_w^e} \mathbf{r}_{ijk}^e L_i^{K_u^e}(u) L_j^{K_v^e}(v) L_k^{K_w^e}(w), \quad -1 \leq u,v,w \leq 1, \tag{2}$$

where $\mathbf{r}_{ijk}^e = \mathbf{r}(u_i, v_j, w_k)$ are position vectors of interpolation nodes and $L_i^{K_u^e}$ represent Lagrange interpolation polynomials,

$$L_i^{K_u^e}(u) = \prod_{\substack{h=0 \\ h \neq i}}^{K_u^e} \frac{u - u_h}{u_i - u_h}, \tag{3}$$

and similarly for $L_j^{K_v^e}(v)$ and $L_k^{K_w^e}(w)$. Eqs. (2) and (3) define a mapping from a cubical parent domain to the generalized hexahedron.

The same polynomials in (3) are used to describe the continuous spatial variations of both the complex relative permittivity and permeability tensors, $\bar{\bar{\varepsilon}}_r$ and $\bar{\bar{\mu}}_r$, of an anisotropic inhomogeneous material filling the generalized hexahedral element in Figure 1 ($e$th element in the model) as follows:

$$\begin{aligned}\bar{\bar{\varepsilon}}_r^e(u,v,w) &= \begin{bmatrix} \varepsilon_{r,xx}^e(u,v,w) & \varepsilon_{r,xy}^e(u,v,w) & \varepsilon_{r,xz}^e(u,v,w) \\ \varepsilon_{r,yx}^e(u,v,w) & \varepsilon_{r,yy}^e(u,v,w) & \varepsilon_{r,yz}^e(u,v,w) \\ \varepsilon_{r,zx}^e(u,v,w) & \varepsilon_{r,zy}^e(u,v,w) & \varepsilon_{r,zz}^e(u,v,w) \end{bmatrix} \\ &= \sum_{m=0}^{M_u^e} \sum_{n=0}^{M_v^e} \sum_{p=0}^{M_w^e} \bar{\bar{\varepsilon}}_{r,mnp}^e L_m^{M_u^e}(u) L_n^{M_v^e}(v) L_p^{M_w^e}(w), \quad -1 \leq u,v,w \leq 1,\end{aligned} \tag{4}$$

where $\bar{\bar{\varepsilon}}_{r,mnp}^e = \bar{\bar{\varepsilon}}_r^e(u_m, v_n, w_p)$ are the relative permittivity values at the points defined by position vectors of spatial interpolation nodes, $\mathbf{r}_{mnp}^e$, and similarly for $\bar{\bar{\mu}}_r^e(u,v,w)$, with $M_u^e$, $M_v^e$, and $M_w^e$ ($M_u^e$, $M_v^e$, $M_w^e \geq 1$) standing for arbitrary material-representation polynomial orders within the element.

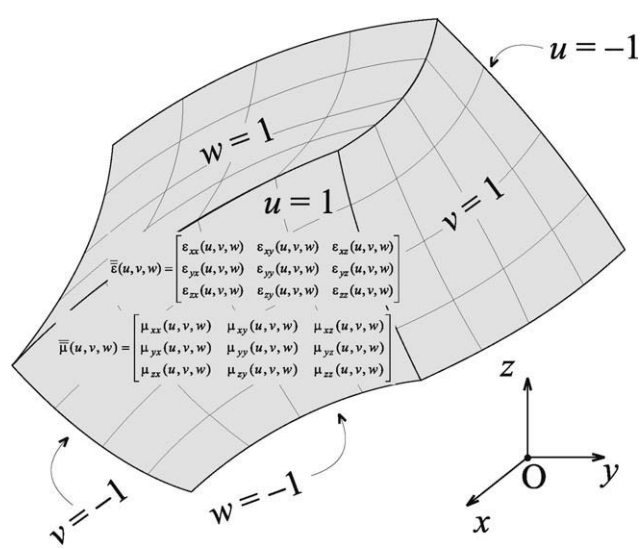


**Figure 1** Generalized curved parametric hexahedron defined by (2), with continuous spatial variations of complex relative permittivity and permeability tensors of the material given by (4)

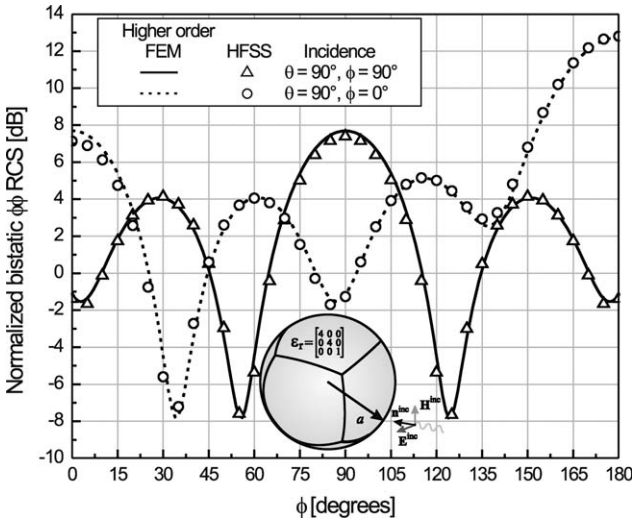


**Figure 2** Bistatic RCS in the $x$–$y$ plane of an anisotropic dielectric spherical scatterer with the relative permittivity tensor given by (10), normalized to $\lambda_0^2$, $\lambda_0$ being the free-space wavelength, for the plane wave incidence from the direction defined by $\theta = 90°$ and $\phi = 90°$ or $\phi = 0°$; higher order FEM–MoM model of the scatterer, with a single finite element, is shown in the figure inset

Basis functions are curl-conforming hierarchical polynomials of arbitrary field-approximation orders $N_u^e$, $N_v^e$, and $N_w^e$ ($N_u^e$, $N_v^e$, $N_w^e \geq 1$) in the $e$th element, in Figure 1, which, for the reciprocal $u$-component of the field vector, are given by [6]

$$\mathbf{f}_{uqst}^e = u^q P_s(v) P_t(w) \frac{\mathbf{a}_v^e \times \mathbf{a}_w^e}{\Im^e}, \quad P_s(v) = \begin{cases} 1 - v, & n = 0 \\ v + 1, & n = 1 \\ v^s - 1, & s \geq 2, \text{even} \\ v^s - v, & s \geq 3, \text{odd} \end{cases},$$

$$\Im^e = (\mathbf{a}_u^e \times \mathbf{a}_v^e) \cdot \mathbf{a}_w^e, \quad \mathbf{a}_u^e = \frac{\partial \mathbf{r}^e}{\partial u},$$

$$\mathbf{a}_v^e = \frac{\partial \mathbf{r}^e}{\partial v}, \quad \mathbf{a}_w^e = \frac{\partial \mathbf{r}^e}{\partial w}, \quad -1 \leq u, v, w \leq 1, \quad q = 0, 1, \ldots, N_u^e - 1,$$
$$s = 0, 1, \ldots, N_v^e, \quad t = 0, 1, \ldots, N_w^e, \tag{5}$$

where $\Im^e$ is the Jacobian of the covariant transformation, and $\mathbf{a}_u^e$, $\mathbf{a}_v^e$, and $\mathbf{a}_w^e$ are the unitary vectors along the parametric coordinates of the element. Higher order hierarchical basis functions with improved orthogonality and conditioning properties constructed from Legendre and other standard orthogonal polynomials [11, 12] may also be implemented.

Geometrical-mapping orders ($K_u^e$, $K_v^e$, $K_w^e$) in (2), material-representation orders ($M_u^e$, $M_v^e$, $M_w^e$) in (4), and field-expansion orders ($N_u^e$, $N_v^e$, $N_w^e$) in (5) are entirely independent from each other, and the three sets of parameters of a higher order model can be combined independently for the best overall performance of the method. Furthermore, because the basis functions in (5) are hierarchical (each lower-order set of functions is a subset of all higher-order sets), all of the parameters can be adopted anisotropically in different directions within an element, and nonuniformly from element to element in a model.

To solve for the field coefficients, $\gamma_l$, we substitute the field expansion (1) in the curl-curl electric field vector wave equation [6], which for the $e$th element reads

$$\nabla \times \left[\bar{\bar{\mu}}_r^{e^{-1}}(u, v, w) \nabla \times \mathbf{E}^e(u, v, w)\right] - k_0^2 \bar{\bar{\varepsilon}}_r^e(u, v, w) \mathbf{E}^e(u, v, w) = 0, \tag{6}$$

with $k_0 = \omega\sqrt{\varepsilon_0 \mu_0}$ being for the free-space wave number. A standard Galerkin weak-form discretization of (6) yields

$$\begin{aligned} &\int_{V^e} \left[\nabla \times \mathbf{f}_t^e(u, v, w)\right] \cdot \left[\bar{\bar{\mu}}_r^{e^{-1}}(u, v, w) \nabla \times \mathbf{E}^e(u, v, w)\right] \mathrm{d}V \\ &- k_0^2 \int_{V^e} \mathbf{f}_t^e(u, v, w) \cdot \left[\bar{\bar{\varepsilon}}_r^e(u, v, w) \mathbf{E}^e(u, v, w)\right] \mathrm{d}V \\ &= \mathrm{j} k_0 \eta_0 \oint_{S^e} \mathbf{f}_t^e(u, v, w) \cdot [\mathbf{n} \times \mathbf{H}^e(u, v, w)] \mathrm{d}S, \end{aligned} \tag{7}$$

where $V^e$ is the volume of the $e$th element, bounded by the surface $S^e$, $\mathbf{n}$ is the outward unit normal on $S^e$, $\mathbf{f}_t$ are testing functions [the same as basis functions in (1) and (5)], and $\eta_0$ is the free-space intrinsic impedance. Because of the continuity of the tangential component of the magnetic field intensity vector, $\mathbf{n} \times \mathbf{H}^e$, in (7) across the interface between any two finite elements in the FEM model, the right-hand side term in (7) contains the surface integral over the overall boundary surface, $S$, of the entire FEM domain, and not over the internal boundary surfaces between the individual hexahedra in the model.

For open-region scattering structures, the FEM domain is truncated at the surface $S$ by means of unknown equivalent surface electric and magnetic currents, of densities $\mathbf{J}_S$ and $\mathbf{M}_S$, respectively, defined on MoM curved quadrilateral patches representing external (on $S$) faces of the FEM hexahedra, and expanded using a divergence-conforming 2D version of basis functions in (5) [10]. The electric field in the FEM domain, $\mathbf{E}_{FEM}$, given by (1) in individual finite elements, is coupled to the scattered electric and magnetic fields due to $\mathbf{J}_S$ and $\mathbf{M}_S$, $\mathbf{E}_{MoM}$ and $\mathbf{H}_{MoM}$, and the incident fields, $\mathbf{E}_{inc}$ and $\mathbf{H}_{inc}$, through boundary conditions for the tangential field components on $S$ as follows:

$$\begin{aligned} \mathbf{n} \times \mathbf{E}_{FEM} &= \mathbf{n} \times \mathbf{E}_{MoM}(\mathbf{J}_S, \mathbf{M}_S) + \mathbf{n} \times \mathbf{E}_{inc}, \\ \mathbf{n} \times \mathbf{H}_{FEM} &= \mathbf{J}_S = \mathbf{n} \times \mathbf{H}_{MoM}(\mathbf{J}_S, \mathbf{M}_S) + \mathbf{n} \times \mathbf{H}_{inc}, \end{aligned} \tag{8}$$

thus, providing the computational interface between the FEM and MoM regions, with $\mathbf{E}_{FEM}$, $\mathbf{J}_S$, and $\mathbf{M}_S$ as unknowns, and giving rise to a hybrid higher order FEM-MoM solution [8].

For closed-region microwave waveguide structures, the right-hand side term in (7) reduces to the surface integral across the artificially introduced planar surfaces (waveguide ports). If, moreover, the waveguide operates in the single-mode regime (which is a standard assumption for practical microwave applications) and the ports are moved away from all discontinuities (by placing a single large finite element with a high field-approximation order in the longitudinal direction as a buffer zone), the boundary condition at the ports is expressed as [1, 7]

$$\begin{aligned} &\mathbf{n} \times (\nabla \times \mathbf{E}_{FEM}) + \mathrm{j} k_{z10} \mathbf{n} \times (\mathbf{n} \times \mathbf{E}_{FEM}) \\ &= \begin{cases} -2\mathrm{j} k_{z10} \mathbf{E}_{inc}, \mathbf{E}_{inc} = \mathbf{E}_0 \exp(-\mathrm{j} k_{z10} z) & (\text{excitation port}) \\ 0 & (\text{receiving ports}) \end{cases}, \end{aligned} \tag{9}$$

where, for a rectangular waveguide, $k_{z10} = \sqrt{k_0^2 - (\pi/a)^2}$ is the wave number of the dominant mode ($a$ is the larger dimension of the waveguide cross section).

## 3. NUMERICAL RESULTS AND DISCUSSION

As the first example of the application of the novel higher order large-domain general FEM technique, aimed at demonstrating the accuracy and efficiency of the technique when curved large

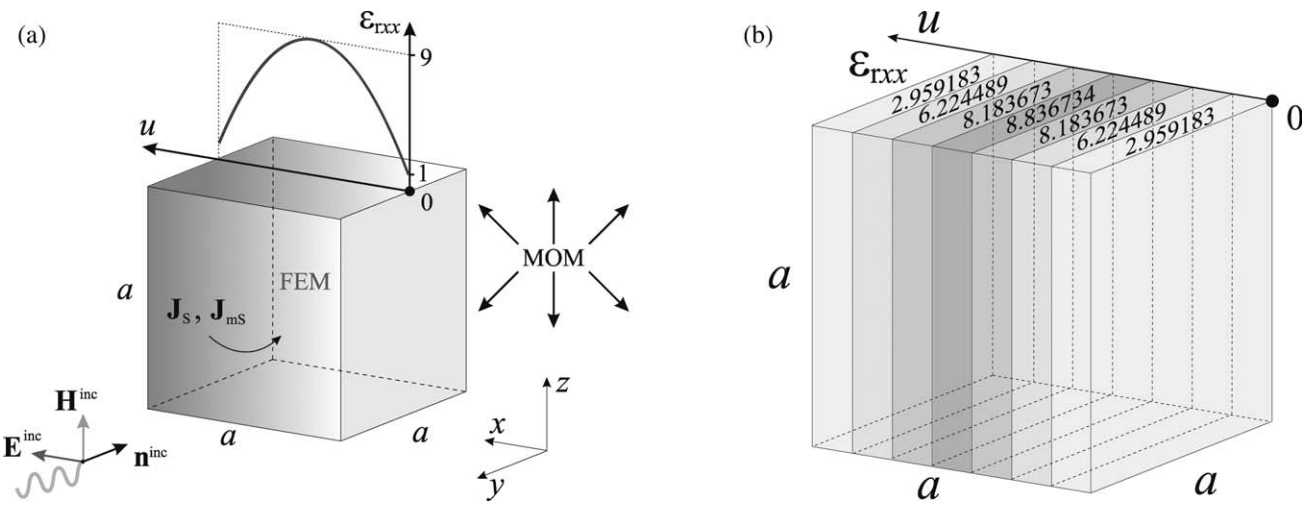


**Figure 3** Analysis of a continuously inhomogeneous anisotropic dielectric cubical scatterer with the relative permittivity tensor given by (11): (a) exact higher order FEM–MoM model with a single finite element and (b) approximate piecewise homogeneous anisotropic model, with averaged permittivities of layers, for HFSS simulation

anisotropic finite elements with $p$-refined field distributions are used, consider an anisotropic dielectric (nonmagnetic and lossless) spherical scatterer, of radius $a = 1$m and relative permittivity given by the tensor

$$\bar{\bar{\varepsilon}}_r = \begin{bmatrix} 4 & 0 & 0 \\ 0 & 4 & 0 \\ 0 & 0 & 1 \end{bmatrix}, \tag{10}$$

illuminated by an incident time-harmonic plane wave of frequency $f = 150$ MHz. Shown in the inset of Figure 2 is the higher order FEM–MoM model of the scatterer, which consists of a single curved hexahedral FEM element and six MoM curved quadrilaterals, all of geometrical-mapping orders $K = 2$. The orders of the polynomial expansion are $N_{\mathrm{FEM}} = 7$ and $N_{\mathrm{MOM}} = 6$ for the fields in the FEM domain and for the surface currents in the MoM domain, respectively. In Figure 2, the bistatic radar cross section (RCS) of the scatterer computed using the higher order FEM–MoM is compared with the results obtained by HFSS, and an excellent agreement of the two sets of results is observed. The described FEM–MoM model results in 1344 FEM and 864 MoM unknowns, while the HFSS simulation, which converges to 0.1 delta energy in six adaptive passes, uses 412,592 first-order tetrahedral finite elements (the number of unknowns is of the same order of magnitude).

As an example of an accurate and efficient higher order large-domain FEM–MoM scattering analysis of continuously inhomogeneous anisotropic structures, we next consider a dielectric cubical scatterer, of side length $a = 1$m, with relative permittivity described by the tensor

$$\bar{\bar{\varepsilon}}_r(u) = \begin{bmatrix} 9 - 8u^2 & 0 & 0 \\ 0 & 1 & 0 \\ 0 & 0 & 1 \end{bmatrix}, \quad -1 \le u \le 1, \tag{11}$$

as shown in Figure 3(a). The scatterer is excited by an incident $\phi$-polarized plane wave from different directions in the $x$–$y$ plane ($\theta = 90°$) at a frequency of $f = 300$ MHz. The FEM–MoM model, in Figure 3(a), consists of a single FEM element of the geometrical order $K = 1$, with the permittivity $\varepsilon_{rxx}$ represented as a Lagrange polynomial function of material-representation order $M = 2$, and six MoM quadrilaterals. The orders of the FEM and MoM field/current polynomial expansions are the same as in the first example. The reference HFSS solutions for validation and comparison are obtained using piecewise homogeneous anisotropic layered approximations of the dielectric profile, with the original structure subdivided into several equally thick anisotropic layers with individual permittivities calculated as the average of the corresponding permittivity functions for the layer, as depicted in Figure 3(b) for the model with seven layers. From the results for the monostatic RCS of the scatterer shown in Figure 4, we see that models with three and five layers provide an inadequate approximation of the continuous permittivity profile of the cube, giving rather inaccurate RCS values, and that seven (and more) layers are necessary to obtain a satisfactory approximation of the profile yielding a quite accurate RCS characterization and a very good agreement of the results obtained by the higher order continuously inhomogeneous anisotropic FEM model and the approximate layered HFSS model.

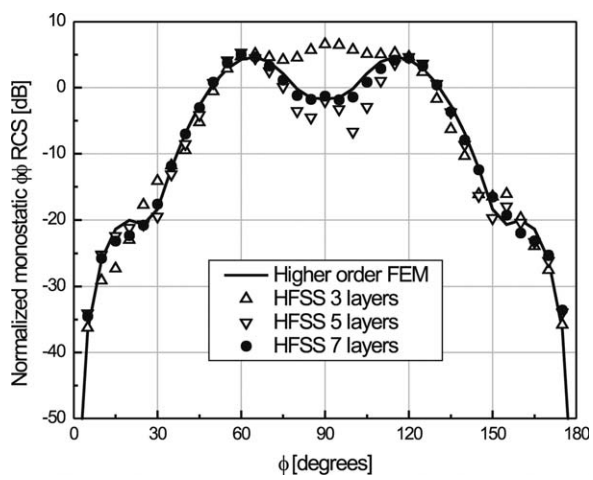


**Figure 4** Normalized monostatic RCS (RCS/$\lambda_0^2$) in the $x$–$y$ plane of the scatterer in Figure 3

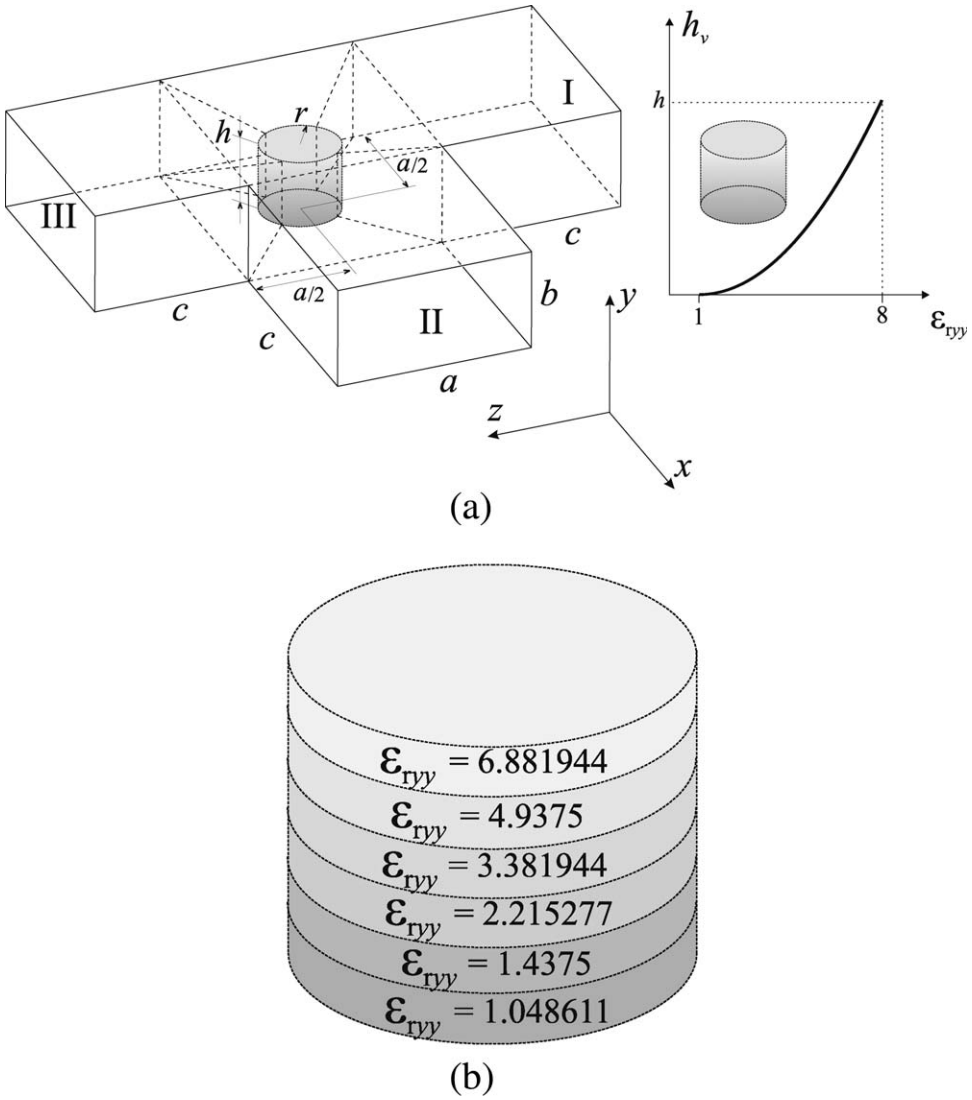


**Figure 5** *H*-plane WR-75 waveguide T-junction with a ''partial-height'' continuously inhomogeneous anisotropic cylindrical dielectric post whose relative permittivity tensor is given by (12): (a) structure geometry ($r = 5$ mm, $h = 6$ mm, $a = 19.05$ mm, $b = 9.525$ mm, and $c = 30$ mm) and higher order large-domain FEM mesh and (b) approximate six-layer model of the post used in HFSS simulations

Finally, to demonstrate an accurate and efficient higher order large-domain FEM analysis of waveguide structures with anisotropic continuously inhomogeneous materials, that also include curvature, the last example is an *H*-plane waveguide T-junction with a ''partial-height'' cylindrical dielectric post, shown in Figure 5(a), with the relative permittivity tensor defined as

$$\bar{\bar{\varepsilon}}_{\mathrm{r}}(v) = \begin{bmatrix} 1 & 0 & 0 \\ 0 & 1 + 7\frac{(v+1)^2}{4} & 0 \\ 0 & 0 & 1 \end{bmatrix}, \quad -1 \le v \le 1, \qquad (12)$$

and the $\varepsilon_{ryy}$ component being represented as the second-order ($M = 2$) Lagrange polynomial. For the reference HFSS simulation, the post is modeled using six layers as depicted in Figure 5(b). A higher order FEM model of the junction and discontinuity consists of three trilinear ($K = 1$) and six triquadratic ($K = 2$) hexahedral finite elements, as portrayed in Figure 5(a), with polynomial field-expansion orders ($N_u^e$, $N_v^e$, and $N_w^e$) in the FEM simulation ranging from 2 to 7 in different elements and different directions. In Figure 6, we observe an excellent agreement

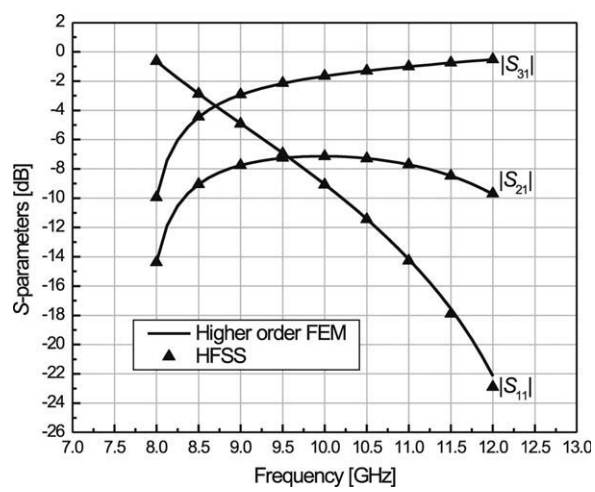


**Figure 6** Magnitudes of *S*-parameters of the waveguide structure in Figure 5

of higher order continuous isotropic FEM and layered anisotropic HFSS results for the $S$-parameters of the structure.

## 4. CONCLUSION

This article has presented a novel higher order large-domain FEM technique for 3D analysis of open- and closed-region electromagnetic structures involving general anisotropic inhomogeneous materials. The technique features Lagrange generalized curved parametric hexahedral finite elements with anisotropic continuously inhomogeneous materials in conjunction with curl-conforming hierarchical polynomial vector basis functions for field expansions. The examples have demonstrated efficient and accurate simulations of anisotropic continuously inhomogeneous scattering and waveguide structures. In the analysis of scatterers, the FEM domain is truncated by a hybridization with a higher order MoM–SIE technique. For multiport waveguide discontinuities, a simple single-mode boundary condition is introduced across the waveguide ports. This appears to be the first demonstration of large (up to a couple of wavelengths across) anisotropic inhomogeneous curved finite elements with $p$-refined high-order (e.g., seventh-order) field distributions for electromagnetic modeling. Our current and future work includes applications of the new elements in electromagnetic cloaking, PMLs, and waveguide component designs.


## ACKNOWLEDGMENTS

This work was supported by the National Science Foundation under grants ECCS-0650719 and ECCS-1002385 and by the Serbian Ministry of Science and Technological Development under grant TR-32005.


## REFERENCES


1. J.M. Jin, The finite element method in electromagnetics, 2nd ed., Wiley, New York, 2002.
2. J.M. Jin and D.J. Riley, Finite element analysis of antennas and arrays, Wiley, New York, 2008.
3. P.P. Silvester and R.L. Ferrari, Finite elements for electrical engineers, 3rd ed., Cambridge University Press, 1996.
4. J.L. Volakis, A. Chatterjee, and L.C. Kempel, Finite element method for electromagnetics, IEEE Press, New York, 1998.
5. B.M. Notaroš, Higher order frequency-domain computational electromagnetics, Special Issue on Large and Multiscale Computational Electromagnetics, IEEE Trans Antennas Propag 56 (2008), 2251–2276.
6. M.M. Ilić and B.M. Notaroš, Higher order hierarchical curved hexahedral vector finite elements for electromagnetic modeling, IEEE Trans Microwave Theory Tech 51 (2003), 1026–1033.
7. M.M. Ilić, A.Ž. Ilić, and B.M. Notaroš, Higher order large-domain FEM modeling of 3-D multiport waveguide structures with arbitrary discontinuities, IEEE Trans Microwave Theory Tech 52 (2004), 1608–1614.
8. M.M. Ilić, M. Djordjević, A.Ž. Ilić, and B.M. Notaroš, Higher order hybrid FEM-MoM technique for analysis of antennas and scatterers, IEEE Trans Antennas Propag 57 (2009), 1452–1460.
9. M.M. Ilić, A.Ž. Ilić, and B.M. Notaroš, Continuously inhomogeneous higher order finite elements for 3-D electromagnetic analysis, IEEE Trans Antennas Propag 57 (2009), 2798–2803.
10. M. Djordjević and B.M. Notaroš, Double higher order method of moments for surface integral equation modeling of metallic and dielectric antennas and scatterers, IEEE Trans Antennas Propag 52 (2004), 2118–2129.
11. M.M. Ilić and B.M. Notaroš, Higher order large-domain hierarchical FEM technique for electromagnetic modeling using Legendre basis functions on generalized hexahedra, Electromagnetics 26 (2006) 517–529.
12. M. Djordjević and B.M. Notaroš, Higher-order hierarchical basis functions with improved orthogonality properties for moment-method modeling of metallic and dielectric microwave structures, Microwave Opt Technol Lett 37 (2003), 83–88.
13. J.B. Pendry, D. Schurig, and D.R. Smith, Controlling electromagnetic fields, Science 312 (2006), 1780–1782.


© 2012 Wiley Periodicals, Inc.

# HIGH GAIN FERMI ANTENNA ARRAY FOR RADAR-AIDED RADIOTHERAPY SYSTEM


**Zeeshan Salmani,[1] Changzhan Gu,[2] Changzhi Li,[2] and Hualiang Zhang[1]**

[1] Department of Electrical Engineering, University of North Texas, Denton, TX; Corresponding author: hualiang.zhang@unt.edu

[2] Department of Electrical and Computer Engineering, Texas Tech University, Lubbock, TX


*Received 14 September 2011*


**ABSTRACT:** *This article presents the design of Fermi antenna array with improved gain for radar respiration measurement. A six-element Fermi antenna array working at 5.8 GHz is optimally designed and integrated with the respiration radar system. Specifically, to easily feed the antenna array as well as reduce the total size of the array system, a feeding network based on 0-degree phase shifters is used along with suitable impedance transformers. The whole system is proposed to function as a radar sensor for respiration rate measurement, which is known as a promising noncontact and noninvasive approach for lung cancer radiotherapy. The measurement results verify the improved performance of the proposed system for radar respiration measurement in motion-adaptive lung cancer radiotherapy.* © 2012 Wiley Periodicals, Inc. Microwave Opt Technol Lett 54:1649–1654, 2012; View this article online at wileyonlinelibrary.com. DOI 10.1002/mop.26871


**Key words:** *Fermi antenna; radar; lung cancer radiotherapy; motion adaptive*

## 1. INTRODUCTION

Radar technologies have been widely used in both civil and military applications including remote sensing [1, 2], search and rescue [3], and imaging [4]. Recently, it has become attractive to apply radar techniques in the clinical sectors, as it will enable noninvasive and noncontact detections of many useful parameters for medical diagnosis and treatment. Following this observation, several radar systems for medical purpose have been developed [5–7]. Among them, one interesting application is for lung cancer treatment. It is known that lung cancer is the leading cause of cancer death in the United States among every ethnic group. It accounts for about 12% of all newly diagnosed cancers, and 28% of all cancer deaths. Currently, radiotherapy is one of the major modalities for lung cancer treatment. However, as lung tumors can move significantly (2–3 cm) with respiration motion, it is very difficult, if not impossible, for existing radiotherapy techniques to deliver sufficient radiation dose without damaging the surrounding healthy lung tissues. To address this issue, radar systems can be used to realize motion-adaptive radiotherapy. In this way, the respiration is dynamically measured and correlated with the radiation beam, allowing a reduction in the volume of healthy tissue exposed to a high dose. A typical schematic of such system is shown in Figure 1. The devised radar is integrated